AGU PUBLICATIONS

JGR

Journal of Geophysical Research: Oceans

RESEARCH ARTICLE

10.1002/2015JC010741

Key Points:
- Snow thickness distributions lead to better simulated light fields in sea ice
- Modeled light fields under distributed snow improve agreement with observations
- Distributed snow explains why models needed effective thermal conductivities

Supporting Information:
- Supporting Information S1
- Figure S1
- Figure S2
- Figure S3
- Figure S4
- Figure S5
- Figure S6

Correspondence to:
C. Abraham,
carsten.abraham@mpimet.mpg.de

Citation:
Abraham, C., N. Steiner, A. Monahan, and C. Michel (2015), Effects of subgrid-scale snow thickness variability on radiative transfer in sea ice, *J. Geophys. Res. Oceans*, *120*, 5597–5614, doi:10.1002/2015JC010741.

Received 22 JAN 2015
Accepted 11 JUL 2015
Accepted article online 16 JUL 2015
Published online 14 AUG 2015

Effects of subgrid-scale snow thickness variability on radiative transfer in sea ice

Carsten Abraham[1], Nadja Steiner[2,3], Adam Monahan[3], and Christine Michel[4]

[1]Max Planck Institute for Meteorology, Hamburg, Germany, [2]Fisheries and Oceans Canada, Institute of Ocean Sciences, Sidney, British Columbia, Canada, [3]University of Victoria, Victoria, British Columbia, Canada, [4]Fisheries and Oceans Canada, Arctic Research Division, Freshwater Institute, Winnipeg, Manitoba, Canada

Abstract Snow is a principal factor in controlling heat and light fluxes through sea ice. With the goal of improving radiative and heat flux estimates through sea ice in regional and global models without the need of detailed snow property descriptions, a new parameterization including subgrid-scale snow thickness variability is presented. One-parameter snow thickness distributions depending only on the gridbox-mean snow thickness are introduced resulting in analytical solutions for the fluxes of heat and light through the snow layer. As the snowpack melts, these snow thickness distributions ensure a smooth seasonal transition of the light field under sea ice. Spatially homogenous melting applied to an inhomogeneous distribution of snow thicknesses allows the appearance of bare sea ice areas and melt ponds before all snow has melted. In comparison to uniform-thickness snow used in previous models, the bias in the under sea-ice light field is halved with this parameterization. Model results from a one-dimensional ocean turbulence model coupled with a thermodynamic sea ice model are compared to observations near Resolute in the Canadian High Arctic. The simulations show substantial improvements not only to the light field at the sea ice base which will affect ice algal growth but also to the sea ice and seasonal snowpack evolution. During melting periods, the snowpack can survive longer while sea ice thickness starts to reduce earlier.

1. Introduction

The Arctic Ocean is a region of particular importance to climate change not only because of the remarkable recent declines in sea ice extent and thickness but also because the marine ecosystem is undergoing profound changes which may feed back on the physical and chemical aspects of the climate system [e.g., *Vaughan et al.*, 2013; *AMAP*, 2013; *Meier et al.*, 2014; *Steiner et al.*, 2015]. Ecosystem responses have already been observed [*Wassmann et al.*, 2011] including, for instance, earlier and larger springtime increases in primary production in open water as well as under the ice [*Arrigo et al.*, 2008; *Arrigo and van Dijken*, 2011; *Arrigo et al.*, 2012]. Changes to the melting and freezing of snow and sea ice have an impact not only on primary production [*Vancoppenolle et al.*, 2013a] but also on other ecosystem processes and higher trophic levels [*Grebmeier et al.*, 2006; *Kovacs et al.*, 2011], for instance an increase in pelagic fish, a reduction of benthic prey, and consequential migration of marine mammal population. The processes behind these changes are complex, and fundamental questions remain regarding the role and the contribution of snow and sea ice to biogeochemical dynamics in the Arctic Ocean [*Vancoppenolle et al.*, 2013b]. In this study, we will address the parameterization of light and heat transfer through snow and sea ice in regional and global models by taking into account subgrid-scale variability of the snow cover. Because these parameterizations are intended for use in regional and global models, they are designed to capture the most important aspects of the snow thickness distribution using standard model fields, rather than including detailed models of snow properties or snow dynamics.

Changing snow and ice conditions affect microbial communities within sea ice (e.g., ice algae) and in the water column below (e.g., pelagic phytoplankton), primarily due to changing light intensity and nutrient availability [e.g., *Søreide et al.*, 2010; *Leu et al.*, 2011; *Bergeron and Tremblay*, 2014; *Ardyna et al.*, 2014]. While ice algae can be found at different levels within the sea ice, the bulk of the biomass is generally concentrated at the bottom, where access to nutrients is most prevalent [*Arrigo*, 2014]. Ice algae can also form aggregates and stringy filaments attached to the bottom of the ice [*Poulin et al.*, 2014]. While heat fluxes are important for the physical properties of sea ice (such as thickness), the light field within and below the ice is of particular importance for biological communities. Springtime reductions in snow and sea ice thickness

[*Anderson and Drobot*, 2001] result in an increase in the light that can penetrate into and pass through the ice affecting timing, quantity, and food quality of primary producers both within and below the sea ice [e.g., *Leu et al*., 2010, 2011; for reviews see *Michel*, 2013; *Meier et al*., 2014; E. Leu et al., Arctic spring awakening-steering principles behind the phenology of vernal ice algae blooms, submitted to *Progress in Oceanography*, 2013].

Previous efforts to model algae in sea ice have identified biases in the representation of available light within and below sea ice as a primary factor in modeled ecosystem misrepresentations [e.g., *Lavoie et al*., 2005; *Pogson et al*., 2011; *Dupont*, 2012]. In particular, these modeling studies could not adequately reproduce observed light levels at the sea ice base during melting conditions. The modeled light levels were lower than observations, resulting in the modeled ice algal bloom occurring later than observed. *Lavoie et al*. [2005] explained the onset bias by the fact that only two values were used for the extinction and transmission coefficients of snow, representing freezing and melting conditions (distinguished by the transition of the surface temperature from below the freezing point to above). They proposed that continuously varying coefficients might improve the representation of the light field. *Pogson et al*. [2011] applied a linear interpolation between the coefficients during transition times but found similar biases. These authors concluded that the snow cover is the principal factor influencing radiative transfer through ice due to its opacity as was also pointed out by *Castro-Morales et al*. [2014]. *Pogson et al*. [2011] pointed out that models do not account for diffusive light from all directions within the ice. *Dupont* [2012] treated the snowpack as opaque and computed available light within and under sea ice as a combination of diffusive light from open leads and snow-free areas but also found a later onset of biomass production than observed. *Frey et al*. [2011] demonstrated that the representation of the light field under sea ice is improved by horizontal propagation of radiation from adjacent melt ponds. Ponded sea ice allows 3–5 times more light to penetrate into sea ice because of a decreased surface albedo [*Light et al*., 2008]. Having developed a simple geometric model that apportions the surface area into bare sea ice and melt ponds, *Frey et al*. [2011] were able to reproduce the light profile in the water column below ponded sea ice late in the melting season when the sea ice is snow free.

While considerable attention has been paid to modeling melt ponds, snow thickness is usually represented as a uniform layer or in terms of complicated subgrid-scale redistributions due to wind processes [e.g., *Lecomte et al*., 2011; *Flocco et al*., 2012; *Hunke et al*., 2013; O. Lecomte et al., Impacts of wind-blown snow redistribution on melt ponds in a coupled ocean-sea ice model, submitted to *Ocean Modelling*, 2014]. This latter class of models are able to capture effects due to different surface types but require many poorly constrained parameters (e.g., for the determination of the specific values of the surface fractions). Furthermore, their greater computational expense reduces the practicality of their implementation in regional or global models. The subgrid-scale structure of the snow field on sea ice, on the other hand, has received little attention. The distribution of snow thickness on sea ice displays strong variability on scales of tens of meters and smaller, influenced by meteorological conditions (e.g., wind-driven redistribution) and the sea ice surface state (e.g., its roughness and topography) [*Iacozza and Barber*, 1999; *Sturm et al*., 2002]. Deeper snow is found where ridged sea ice is present as irregularities in the sea ice surface catch wind-blown snow more effectively. *Iacozza and Barber* [1999] examined the distribution of snow on sea ice and found that the areal average of light transmission is substantially affected by spatial variations in snow thickness around the spatial mean. The temporal evolution of the snowpack is poorly understood due to a lack of continuous snow thickness measurements on sea ice. Snowfall and the formation of the snowpack on sea ice has been found to occur primarily in fall and spring during a small number of snowfall events [*Warren et al*., 1999; *Sturm et al*., 2002]. *Iacozza and Barber* [2009] used the distributed snow-evolution model of *Liston and Elder* [2006] to estimate the spatial and temporal evolution of snow over land-fast sea ice. Even though the model has been successfully used for glaciers [*Mernild et al*., 2007, 2008], on sea ice it showed discrepancies between modeled and observed snow thickness distributions. *Castro-Morales et al*. [2014] point out the high sensitivity of Arctic sea ice growth to the redistribution of snow and sea ice. Despite the demonstrated need, incorporating detailed, process-based subgrid snow thickness models into regional or global climate models is not practical because of their computational expense. Hence, to account for the subgrid-scale snow thickness variability in such models, it is convenient to use a specified probability distribution conditioned on the (resolved) spatial mean.

A number of empirical studies have found that the premelt distribution of snow water equivalent (SWE) depth over reasonably homogenous land surfaces can be approximated by a two-parameter lognormal probability density function [e.g., *Donald et al*., 1995; *Shook*, 1995; *Essery et al*., 1999; *Faria et al*., 2000].

Mathematical considerations of subgrid-scale-distributed snow of homogenous (spatially uniform) as well as inhomogeneous (spatially variable) melt were considered by *Essery and Pomeroy* [2004]. *Liston* [2004] used a lognormally distributed subgrid-scale snow thickness parameterization with uniformly melting snow to average energy and moisture fluxes at the terrestrial-atmosphere interface. The present study is the first to consider the effect of prescribed subgrid-scale snow thickness distributions on light and heat fluxes through sea ice. To keep the parameterization as simple as possible, only distributions determined by a single parameter (the areal mean snow thickness) will be considered. The simplicity of these distributions allows us to obtain analytic expressions for the area-averaged light and heat fluxes. Factors other than the thickness distribution affect light transmission through the snow (e.g., liquid water content, density, and snow type). As a detailed accounting of these effects would require the introduction of new state variables and considerably complicate the parameterization, we do not account for them.

In section 2, subgrid-scale parameterizations of snow thickness distribution are introduced and compared with observed snow distributions, and the effect of subgrid-scale-distributed snow on the radiative and heat fluxes are computed. The influence on radiative and heat fluxes are examined in a coupled 1-D sea ice ocean model described in section 3. Section 4 compares model simulations to observations from a land-fast ice station in Resolute Passage in the Canadian Arctic Archipelago from 2002 [*Lavoie et al*., 2005]. The potential of this subgrid-scale parameterization and suggestions for future research are discussed in section 5 followed by conclusions in section 6.

2. Snow Thickness Distributions

Subgrid-scale snow thickness distributions are prescribed in a manner similar to that of *Liston* [2004]. In contrast to earlier studies in which a two-parameter lognormal probability density function (pdf) was chosen describing subgrid-scale snow variability, families of one-parameter pdfs are applied here. These distributions are specified by the gridbox-mean snow thickness (such as would be resolved in a regional or global model). We do not know from first principles what mathematical form the snow thickness pdf should take. In order to assess the sensitivity of light and heat fluxes to the details of the thickness distribution parameterization, two families of distributions are examined: the Rayleigh distribution and the gamma distribution with a shape parameter equal to 2. The Rayleigh distribution is described as

$$pdf(h) = \frac{\pi h}{2h_s^2} \exp\left(-\frac{\pi h^2}{4h_s^2}\right), \tag{1}$$

where h is the snow thickness and h_s the mean snow thickness. The gamma distribution is described as

$$pdf(h) = \frac{4h}{h_s^2} \exp\left(-\frac{2h}{h_s}\right). \tag{2}$$

These specific distributions were selected because they allow for analytic expressions of the gridbox-mean light and heat fluxes, and because of their similarity to observed snow thickness distributions. Observations taken during the Surface Heat Budget of the Arctic Ocean (SHEBA) experiment [cf. *Sturm et al*., 2002, Figure 7] display a unimodal and positively skewed distribution. Measurements taken by *Kwok et al*. [2011] and *Kurtz and Farrell* [2011] in the Arctic as well as *Worby et al*. [1996] and *Massom et al*. [1998, 2001] in Antarctica agree with these general characteristics of the snow thickness distribution on sea ice. To further investigate the pdf of snow thickness, we obtained observations of snow thickness on Arctic sea ice from the National Aeronautics and Space Administration (NASA) IceBridge missions (National Snow and Ice Data Center [NSIDC]) [*Kurtz et al*., 2012]. These measurements are from the Beaufort Sea, the Canadian Arctic Archipelago, and the western Arctic Ocean in March and April of 2009–2012. Figure 1 shows a histogram of measured snow thicknesses over these 4 years compared to the best fit lognormal distribution (black curve) used in former studies [e.g., *Donald et al*., 1995; *Essery et al*., 1999; *Liston*, 2004], as well as Rayleigh and gamma pdfs (red and blue curves, respectively). The mean observed snow thickness is 0.23 m. Note that fitting the lognormal distribution to the observed data requires the estimation of two parameters, whereas only one parameter each is needed for the Rayleigh and gamma distributions. The single-parameter families of distributions examined here provide reasonable representations of the spatial variability of snow thickness. Although the Rayleigh distribution has its peak at a higher snow thickness and a lower skewness than the observed data shown, for certain mission flights the Rayleigh distribution fits the snow distribution better than the gamma distribution (not shown).

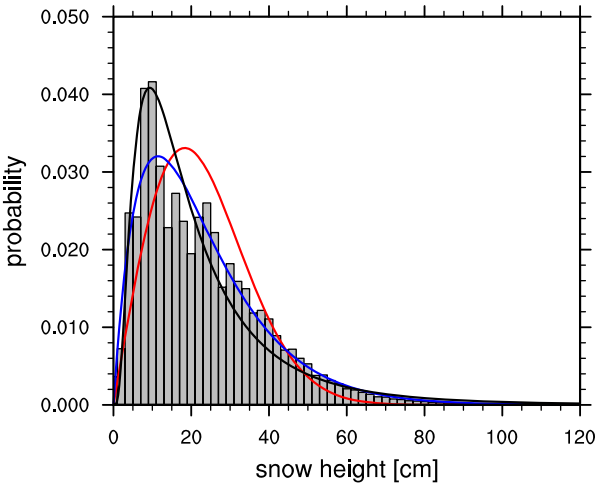

Figure 1. Histogram of the probability density function (pdf) of snow thickness for NASA IceBridge observations from March and April between 2009 and 2012 and estimates for lognormal (black), gamma (blue), and Rayleigh (red) pdfs.

In this study, the attenuation of light due to absorption and scattering as it passes through snow and sea ice is quantified by the simplified radiative transfer equation, as described by the Beer-Lambert law

$$I(z)=I_0\exp(-\kappa z), \tag{3}$$

where $I(z)$ is the radiation at distance z below the surface, I_0 the net radiation penetrating below the surface, and κ the extinction coefficient of the medium. Hereafter, the indices *s* and *sfs* denote snow and snow-free surface values. The radiation incident at the snow surface (or the snow-free parts of the surface during the melt season) is partially reflected and absorbed in the surface layer:

$$I_0=S(1-\alpha)i_0, \tag{4}$$

where S is the shortwave radiation flux incident at the surface, α the albedo, and i_0 the transmissivity coefficient. Note that various interpretations of i_o exist in the literature, some of which imply a finite-depth surface scattering layer, others an infinitesimally thin layer. Throughout this study, we apply the latter interpretation based on the notion that this layer is generally very small when compared to the overall thickness. For snow of nonuniform thickness, the gridbox-mean light intensity $\bar{I}$ under freezing conditions at the snow base is obtained by averaging the Beer-Lambert law over all snow thicknesses weighted by the relative probabilities:

$$\bar{I}=I_0\int_0^\infty pdf(h)\exp(-\kappa_s h)\mathrm{d}h. \tag{5}$$

The use of this average is appropriate when the horizontal length scale of the model gridbox is much larger than the spatial decorrelation scale of the snow thickness (so the gridbox-mean and the population mean are the same). Observations made during SHEBA indicate that this decorrelation scale is about 20 m, independent of the sea ice type [*Sturm et al.*, 2002]. For the Rayleigh distribution, $\bar{I}$ at the snow base is therefore described by

$$\bar{I}=I_0\left(1-\kappa_s h_s\mathrm{erfc}\left(\frac{\kappa_s h_s}{\sqrt{\pi}}\right)\exp\left(\frac{\kappa_s^2 h_s^2}{\pi}\right)\right), \tag{6}$$

where erfc is the complementary error function. Details of this and subsequent calculations are presented in the supporting information. For the gamma distribution $\bar{I}$ is

$$\bar{I}=I_0\frac{4}{h_s^2}\left(\frac{2}{h_s}+\kappa_s\right)^{-2}. \tag{7}$$

Both subgrid-scale snow thickness distributions yield values for $\bar{I}$ at the snow base that are larger than $I_0\exp(-\kappa_s h_s)$, the value corresponding to uniform-thickness snow. The physical reason for this effect is that the transmission of light through snow decreases rapidly as the snow thickness is increased, so the contributions to areally averaged transmission are dominated by regions where the snow thickness is less than the mean.

The full range of distributions (1) or (2) are used during periods of snow growth, or when the snow thickness is not changing with time. Similarly to *Liston* [2004], under melting conditions the distributions are modified. It is assumed that the melt is spatially uniform across the entire gridbox so the same amount of snow is removed from each thickness range. As a result, the distributions are shifted along the h axis toward $h=0$ and a snow-free area is formed. The amount ϵ by which the distributions need to be shifted is determined by requiring that the mean of the shifted distributions equals the resolved gridbox-mean:

$$pdf(h) \rightarrow pdf(h+\epsilon)$$

such that

$$\bar{h} = \int_0^\infty h\, pdf(h+\epsilon)\mathrm{d}h.$$

The radiation reaching the topmost sea ice layer under melting conditions is then an area weighted mean of the radiation which has passed through snow and the radiation that encounters a snow-free surface. The snow-free area fraction is given by $1 - A_s$, where A_s is the area fraction which is still covered by snow:

$$A_s = \int_\epsilon^\infty pdf(h)\mathrm{d}h, \tag{8}$$

and the radiation at the sea-ice surface is

$$\bar{I} = I_{0,sfs}\, A_{sfs} + I_{0,s}\, A_s \int_0^\infty pdf(h+\epsilon)\exp(-\kappa_s h)\mathrm{d}h. \tag{9}$$

A_s for the Rayleigh distribution with $\epsilon = 2h_s/\sqrt{\pi} \times \mathrm{erfc}^{-1}(\bar{h}/h_s)$ (supporting information equation (12)) is given by

$$A_s = \exp\left(-\left(\mathrm{erfc}^{-1}\left(\frac{\bar{h}}{h_s}\right)\right)^2\right), \tag{10}$$

where h_s is now the most recent mean thickness reached during freezing conditions, and for the gamma distribution with $\epsilon = -h_s/2 \times (W_{-1}(-2\bar{h}/(h_s e^2)) + 2)$ (supporting information equation (28)) by

$$A_s = \exp\left(\mathrm{W}_{-1}\left(-\frac{2\bar{h}}{h_s \mathrm{e}^2}\right) + 2\right) \cdot \left(-\mathrm{W}_{-1}\left(-\frac{2\bar{h}}{h_s \mathrm{e}^2}\right) - 1\right), \tag{11}$$

where W_{-1} is the lower branch Lambert W function [*Corless et al.*, 1996]. While the Lambert W function is usually not an intrinsic function in compilers a number of approximations are available. Throughout this study the approximation by *Barry et al.* [1993] is used.

The radiation at the ice interface for the Rayleigh distribution is then given by

$$\bar{I} = I_{0,sfs}\, A_{sfs} + I_{0,s}\, A_s \left[\exp\left(-\left(\mathrm{erfc}^{-1}\left(\frac{\bar{h}}{h_s}\right)\right)^2\right) - \exp\left(\frac{2h_s\kappa_s}{\sqrt{\pi}}\mathrm{erfc}^{-1}\left(\frac{\bar{h}}{h_s}\right) + \frac{\kappa_s^2 h_s^2}{\pi}\right) \cdot \kappa_s h_s \mathrm{erfc}\left(\mathrm{erfc}^{-1}\left(\frac{\bar{h}}{h_s}\right) + \frac{\kappa_s h_s}{\sqrt{\pi}}\right)\right], \tag{12}$$

and for the gamma distribution by

$$\bar{I} = I_{0,sfs}\, A_{sfs} + I_{0,s}\, A_s \frac{4}{h_s^2} \cdot \exp\left(W_{-1}\left(-\frac{2\bar{h}}{h_s e^2}\right) + 2\right)\left(\frac{2}{h_s} + \kappa_s\right)^{-1}\left(-\frac{h_s}{2}\left(W_{-1}\left(-\frac{2\bar{h}}{h_s e^2}\right) + 2\right) + \left(\frac{2}{h_s} + \kappa_s\right)^{-1}\right). \tag{13}$$

Freezing and melting periods can alternate during the season in which snow is present. Melting always shifts the snow thickness pdf to the left with positive values of ϵ, creating or increasing the extent of snow-free areas. The change of the snow thickness pdf when freezing follows melting depends on the size of the snow-free area. If the snow-free area fraction is nonzero then the snow thickness pdf is shifted with a negative value of ϵ to produce the correct mean value. That is, snow accumulation is treated as a reversal of the melting process. When the snow-free area is zero, ϵ is zero and increases in mean snow thickness result in changes of the parameter h_s in the Rayleigh or gamma distribution. The artificial snow accumulation treatment in a refreezing cycle can be justified by the fact that melting occurs rarely in a freezing period and if it happens effects on the developing bare-ice area are small. Freezing periods in the melting season are usually not accompanied with snow accumulation since the snowpack builds up primarily in the winter [*Sturm et al.*, 2002].

The conductive heat flux is also affected by the snow distributions. The steady state, one-dimensional conductive heat flux across a snow layer above an ice layer of thickness h_i (each with uniform conductivity) is described by

$$Q = k_s(T_a - T_B)\frac{1}{h_s + \frac{k_i h_i}{k_s}}, \tag{14}$$

where k_s and k_i are thermal conductivities of snow and sea ice, respectively, T_a the atmospheric temperature at the surface, and T_B the temperature at the base of the ice layer (see section 5 of supporting information). In our implementation, h_i is the thickness of the first layer of 10 sea ice layers and T_B its temperature. Following the same line of reasoning used to compute the gridbox-mean light fields, the gridbox-mean conductive heat flux $\bar{Q}$ under freezing conditions does not yield analytical solutions in terms of elementary functions. Exact implementation of these results could be computationally prohibitive. However, in the limit that the mean snow thickness is thicker than the uppermost sea ice layer, which is the case in multilayer sea ice models, $\bar{Q}$ for Rayleigh-distributed snow is well approximated by

$$\bar{Q} = \frac{\pi}{2} k_s \frac{T_a - T_B}{h_s} = \frac{\pi}{2} Q_u, \tag{15}$$

where Q_u is the conductive heat flux that would result from spatially uniform snow of thickness h_s. For the gamma distribution the approximation is

$$\bar{Q} = 2k_s \frac{T_a - T_B}{h_s} = 2Q_u. \tag{16}$$

During freezing conditions $\bar{Q}$ can therefore be described by a multiple of the thermal conductivity under uniform-thickness snow. This result may explain why thermodynamic sea ice models have historically used a higher value for the thermal conductivity of snow, the so-called effective thermal conductivity, than a measured conductivity to produce realistic sea ice growth. Sea ice models commonly use a value of about 0.31 W m^{-1} K^{-1} for k_s, taken from the formulation of *Abels* [1892] for a standard snow density of 330 kg m^{-3}. Measurements by *Sturm et al.* [1997], however, indicate that this value is overestimated (although it should be noted that they examined mostly depth hoar of subarctic taiga which is one of the snow types with the lowest thermal conductivity) [*Domine et al.*, 2011a]. *Lecomte et al.* [2013] compared several parameterizations for the thermal conductivity but all showed thermal conductivities for standard snow density of about half the value used in sea ice models. Our results suggest that accounting for subgrid-scale snow distributions can explain why thermal conductivities need to be increased by roughly a factor of two above measured values when subgrid-scale variations in snow thickness are neglected. In addition, the effective thermal conductivity used in models also includes the effects of sublimation, condensation and effects due to wind processes [e.g., *Ebert and Curry*, 1993]. However, those contributions are small compared to k_s and can be easily added to a parameterization with subgrid-scale snow distributions.

Under melting conditions the problem is more complicated. Following the same line of reasoning as before, integrals of the distributions considered here do not yield closed-form analytical solutions and can only be approximated. However, $\bar{Q}$ through snow under melting conditions is rather small since the sea ice and snow adopt the melting temperatures relatively fast. Therefore, temperature gradients and the associated conductive heat fluxes are negligible. Many sea ice models assume that under melting conditions the temperature gradients within the sea ice vanish. Thus, during melting, changes of the internal energy of sea ice are dominated by irradiance fluxes which is why an accurate simulation of the surface properties and areal fraction changes due to snowmelt is more important than detailed conductive heat flux expressions. From a modeler's perspective the more complete expression for $\bar{Q}$ derived in the supporting information results in a potentially significant increase in computational burden with a marginal improvement of the heat flux. In consequence, we simply assume that heat fluxes through the snow and ice vanish during melting conditions.

Figure 2 illustrates the changes to the snow base light field under subgrid snow distributions for Rayleigh and gamma-distributed snow (equations (6) and (7) for freezing conditions; equations (12) and (13) for melting conditions) relative to uniform-thickness snow (equation (3)). To illustrate the changes in light under melting conditions, the specific case of an initial mean snow thickness of 0.35 m is considered. Albedos,

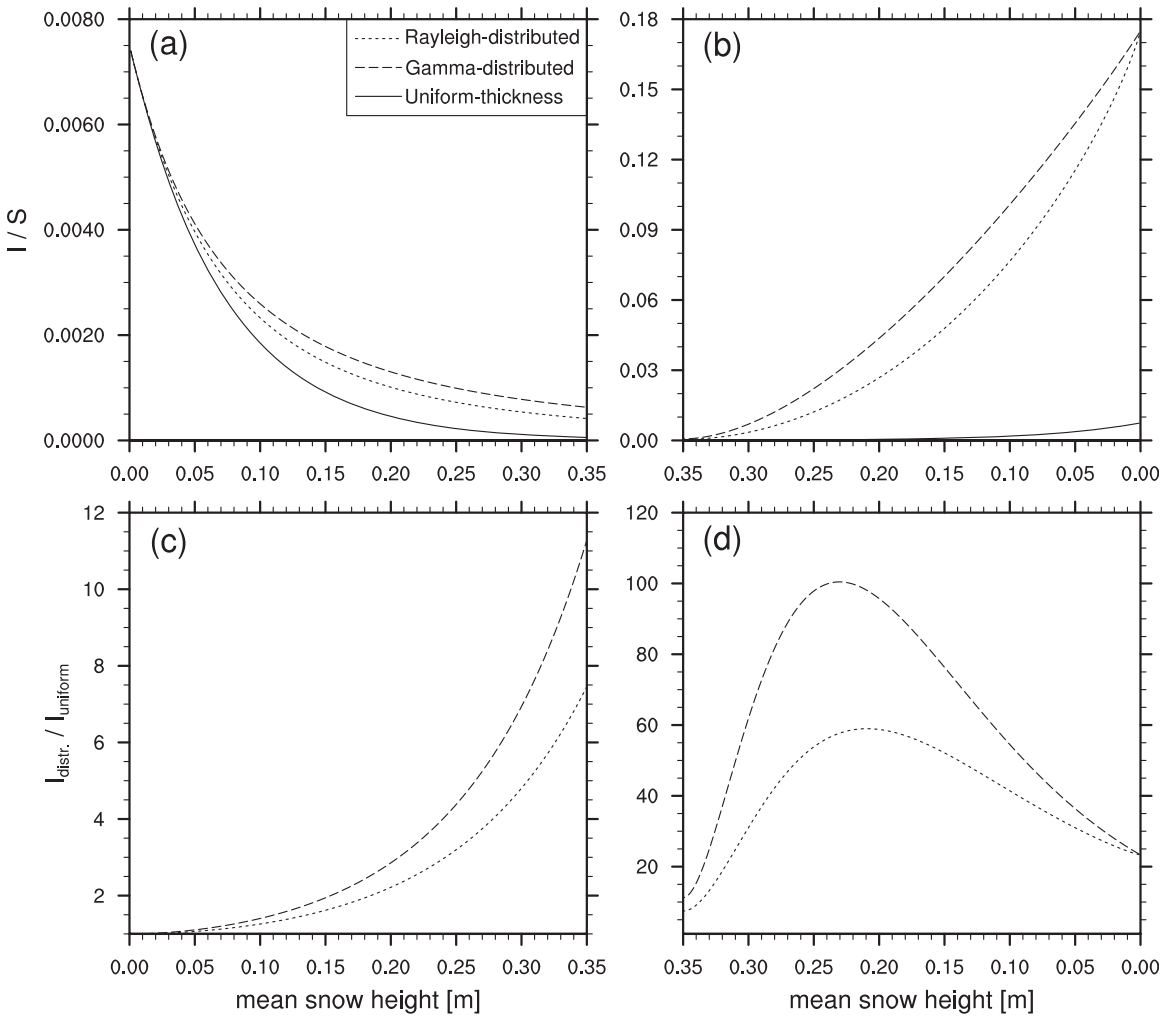

Figure 2. (top) Ratio of transmitted shortwave radiation at the snow-sea-ice interface to incoming shortwave radiation for uniform-thickness snow (solid), Rayleigh-distributed snow (dotted), and gamma-distributed snow (dashed) under (a) freezing and (b) melting conditions. The melting conditions start with a mean snow thickness of 0.35 m. (bottom) Ratio of transmitted shortwave radiation at the uppermost ice layer for Rayleigh-distributed (dotted) and gamma-distributed (dashed) snow to transmitted radiation at the same level under uniform-thickness snow under (c) freezing and (d) melting conditions.

extinction and transmissivity coefficients used are summarized in Table 1. Despite the fact that these coefficients differ between freezing and melting conditions, we choose to compare freezing and melting conditions exclusively with freezing coefficients in order to clearly distinguish effects of the pdf assumptions and optical properties. Under freezing conditions, the difference in light levels for mean snow thicknesses less than 0.05 m is negligible. However, for mean snow thicknesses exceeding 0.15 m for gamma-distributed snow and approximately 0.18 m for Rayleigh-distributed snow the radiation reaching the sea ice is doubled (Figure 2c). These differences become even more pronounced as the mean snow thickness increases. During melting, the radiation at the snow base is up to 60 (100) times higher for Rayleigh-distributed (gamma-distributed) snow (Figure 2d; note the change of scale between left and right-hand plots). As the snowmelts the influence of subgrid-scale snow thickness variability becomes even more pronounced. Accounting for coefficients for melting conditions the effect is still substantial but weaker. The light intensity is still up to 9 (14) times higher for Rayleigh-distributed (gamma-distributed) snow (not shown). An important aspect of the large increase in light when accounting for subgrid snow distributions is the formation of snow-free areas during the melting process. The smooth transition from snow-covered to snow-free conditions results in a smooth transition in light levels as melting starts. This smooth transition was absent in previous treatments in which at the effective snow thickness of 0 m the transmissivity and conductivity of uniform-thickness snow were changed as step functions, i.e., the whole area becomes instantaneously snow free and suddenly different surface conditions apply. How effectively snow attenuates the light can be seen in

Table 1. Extinction and Transmissivity Coefficients Used Throughout This Study and Surface Albedos Used in Section 2

Quantity	Value	Reference
Extinction coefficient freezing snow	14 m^{-1}	*Grenfell and Maykut* [1977]
Extinction coefficient melting snow	7.5 m^{-1}	*Grenfell and Maykut* [1977]
Extinction coefficient freezing sea ice	1.2 m^{-1}	*Smith et al.* [1988]
Extinction coefficient melting sea ice	0.8 m^{-1}	*Light et al.* [2008]
Transmissivity coefficient freezing snow	0.05	*Huwald et al.* [2005]
Transmissivity coefficient melting snow	0.08	*Huwald et al.* [2005]
Transmissivity coefficient freezing sea ice	0.5	*Lavoie et al.* [2005] and *Pogson et al.* [2011]
Transmissivity coefficient melting sea ice	0.5	*Lavoie et al.* [2005] and *Pogson et al.* [2011]
Albedo freezing snow	0.85	*Grenfell and Maykut* [1977]
Albedo melting snow	0.75	*Grenfell and Maykut* [1977]
Albedo freezing sea ice	0.65	*Perovich et al.* [2002b]
Albedo melting sea ice	0.55	*Perovich et al.* [2002b]
Albedo melt ponds	0.3	*Light et al.* [2008]

the limit of no snow under melting conditions (Figures 2b and 2d) because only a few millimeters of snow with uniform thickness attenuate light by a factor of more than 20 times greater than a combination of snow and snow-free areas. Of course, the ratio between distributed snow and uniform-thickness snow jumps to one in the absence of snow.

The results displayed in Figure 2 were obtained assuming that the snow-free areas consist of bare ice. In reality, these areas will generally be partially covered with melt ponds which darken the surface and increase the flux of light into the ice. The effect of melt ponds will be included in the single-column model simulations described below.

3. One-Dimensional Ice-Ocean Model Description

To evaluate the influence of the new representation of the light field and heat fluxes on simulated physical processes, the parameterizations were implemented in the 1-D marine boundary layer model GOTM 3.0 [*Burchard et al.*, 1999; see http://www.gotm.net] coupled to the sea ice model by *Flato and Brown* [1996]. The ocean component was run with configurations and modifications as described in *Steiner et al.* [2006, 2007]. The ocean boundary layer model drives an ecosystem model and calculates surface gas fluxes, with some feedback to the vertical temperature structure through attenuation of penetrating shortwave radiation (equation (1)). In these simulations, GOTM is applied at Resolute, Nunavut, Canada (74°41′51″N, 94°49′56″W), with no Ekman pumping applied. The oceanic time step is 10 min and the vertical domain is 100 m with 1 m resolution. Temperatures and salinities over the whole domain are restored to data from a regional model based on NEMO (Y. Lu, personal communication, 2010) with a 30 day restoring time scale. For the bottom 10 m, the restoring time scale is set to 1 day. Details of the ecosystem model are not relevant to this study and are described elsewhere. The model is forced with hourly averaged atmospheric observations at Resolute from the Canadian Climate Sensor website (http://climate.weather.gc.ca/index_e.html). Daily averaged cloud cover was obtained from corresponding satellite measurements (Clouds and the Earth's Radiant Energy System [CERES] - SYN1deg-M3Hour Ed3A) [*Wielicki et al.*, 1996]. The wavelength range considered is that of photosynthetically active radiation (PAR) from 400 to 700 nm that drives photosynthesis. The sea ice model includes one snow layer and 10 sea ice layers. The original *Flato and Brown* [1996] model was modified to include the subgrid-scale snow thickness distribution discussed in section 2, melt ponds (described below), and temperature-dependent interpolations between melting and freezing periods for extinction and transmission coefficients. Light penetration into the sea ice slab and the conductive heat flux are computed as areally weighted means over regions of bare sea ice, melt pond, or distributed snow.

Flato and Brown [1996] used bulk values for extinction and transmission coefficients of both snow and sea ice. Snow was assumed to be opaque and all shortwave radiation was absorbed in the sea ice. Following the work by *Zeebe et al.* [1996] we assume that only PAR penetrates into the ice interior, with a transmission coefficient that is wavelength-independent. The remaining wavelengths are absorbed in the uppermost layer of the snow or exposed sea ice and contribute to the surface energy budget. This approximation is reasonable to leading order because the wavelength dependence of extinction coefficients in the PAR wave band is weak, while the coefficients increase rapidly above 700 nm [*Grenfell and Maykut*, 1977]. The

extinction and transmissivity coefficients used in this model are listed in Table 1. These values differ between freezing and melting conditions because of the changes in the wetness of the snow and porosity of sea ice. An exception is the transmissivity coefficient for sea ice which is equal under both conditions [e.g., *Lavoie et al.*, 2005; *Pogson et al.*, 2011]. In order to achieve a smooth transition between the various coefficients under conditions of freezing and melting the following temperature dependence is specified

$$c(T) = \frac{c_f + c_m}{2} + \frac{c_m - c_f}{2} \tanh\left(\alpha_c (T - 273.15)\right), \tag{17}$$

where c denotes the varying coefficient with the indices f and m denoting freezing and melting conditions. The quantity α_c is a transition scale parameter with units K^{-1}. Larger values of α_c result in a more abrupt transition between freezing and melting conditions. Throughout this study α_c is set to 1 K^{-1}.

For investigations of the thermodynamic fields of sea ice under subgrid-scale snow thickness distributions the snow density-dependent thermal conductivity parameterization by *Ebert and Curry* [1993] (producing values for k_s between 0.31 and 0.35 W m^{-1} K^{-1} depending on the surface temperature) is replaced with the parameterization by *Domine et al.* [2011b] (values for k_s ranging between 0.15 and 0.17 W m^{-2} K^{-1}). Simulations with uniform-thickness snow still use the effective thermal conductivity given by *Ebert and Curry* [1993] to avoid an underestimation of sea ice thickness. As shown in section 2 the subgrid-scale snow distributions result in an increase of the gridbox-mean thermal conductivity.

Incorporation of subgrid-scale snow distributions discussed in section 2 results in the presence of different surface conditions during the melting season. In addition to bare sea ice and snow-covered areas, melt ponds were introduced to further improve the simulation of the temporal evolution of the sea ice surface conditions as demonstrated in several recent studies [e.g., *Lecomte et al.*, 2011; *Flocco et al.*, 2012; *Hunke et al.*, 2013; Lecomte et al., submitted manuscript, 2014]. These models use more sophisticated melt-pond parameterizations than the one introduced here, however, the focus of this study is how subgrid-scale snow thickness distributions influence the representation of heat fluxes and of light fields within the sea ice. These presented melt-pond parameterization can easily be replaced by more comprehensive melt-pond parameterizations. In our parameterization, melt ponds are produced exclusively by the melting of snow. This assumption can be justified by the fact that melt ponds are observed to reach their maximal areal coverage on average 10 days after the melting of the snowpack has started [*Derksen et al.*, 1997]. This is a time period where residual snow is still present and the sea ice thickness has not decreased. Melt ponds allow more light to penetrate into the sea ice slab because of their relatively low albedo. For simplicity, this study accounts for melt ponds with a modification of the surface energy budget. While melt-pond albedos vary depending on the underlying sea ice conditions, we apply a melt-pond albedo of 0.3 and a transmissivity coefficient of 0.5 [*Light et al.*, 2008; *Grenfell and Maykut*, 1977]. In simulations with snow thickness distributions, we assume that melt ponds accumulate exclusively on snow-free areas as being the lowest surface where meltwater can flow to, which then consist of bare-ice and melt-pond area fractions. A conceptual model description of the subgrid surface properties is presented in Figure 3. Since melt ponds are not observed to cover the entire sea ice area, we include a maximum melt-pond area fraction in our parameterization. Melt-pond areas slightly exceeded 20% spatial fraction on multiyear sea ice during the SHEBA experiment [*Perovich et al.*, 2002a; *Vancoppenolle et al.*, 2013b]. From remote sensing, a total spread of about 25–30% over Arctic sea ice was found [*Rösel and Kaleschke*, 2012]. Hence, we adopt a maximum areal fraction of 30% in this study.

In the case of uniform-thickness snow, there are no snow-free areas until the snow has completely melted (at which point the entire ice surface is snow free). Since the nature of the uniform-thickness snow parameterization does not allow for a redistribution of snow mass, melt ponds are set to form on top of the snow surface. By the time all the snow has melted the residual melt ponds are set to remain on the bare sea ice. Melt ponds are set to a constant maximal melt-pond area fraction as soon as meltwater is produced. The optical properties of melt ponds are identical to those described before, i.e., energy fluxes are a superposition of radiation through the melt pond, snow and ice, or once all snow has melted through the melt ponds and the ice.

As melting progresses, sea ice becomes more porous and the melt ponds drain water into the ocean [*Perovich et al.*, 2003]. Since observations reveal an approximately constant net upward motion of sea ice floes during melting [*Perovich et al.*, 1999], it has been suggested that the drainage rate of melt ponds is approximately constant in time. Following *Taylor and Feltham* [2004], a drainage rate of 0.0175 m d^{-1} is adopted. The change in melt-pond depth h_m is thus given by

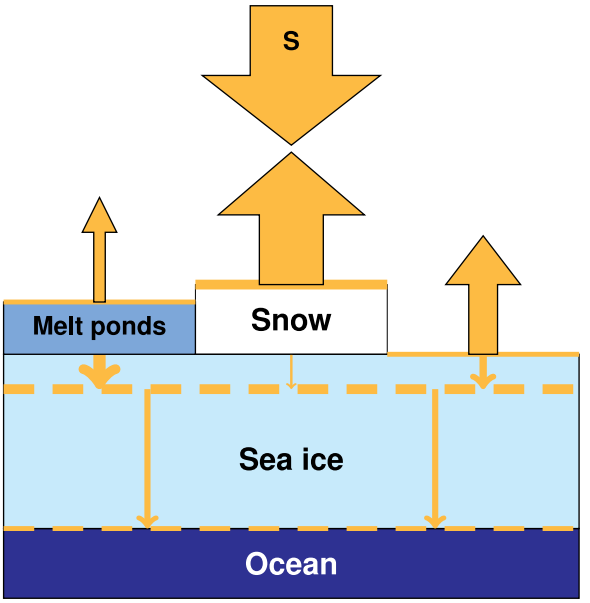

Figure 3. Conceptual illustration of the surface conditions during melting for a subgrid-scale snow distribution. Reflected shortwave radiation from the surface varies under different surface conditions. Arrows indicate various levels of light transferred and reflected by different surface conditions. The light levels are averaged by area fractions to produce a uniform light level within the first sea ice layer. The light thus attenuates further as it passes through the sea ice. For the parameterization with uniform-thickness snow, snow covers the whole area and melt ponds form on top of the snow layer with a fixed melt-pond area fraction.

$$\frac{dh_m}{dt} = \frac{\rho_s}{\rho_w \cdot A_m}\frac{dh_s}{dt} - \beta, \tag{18}$$

where ρ_s is the density of snow, ρ_w the density of freshwater, and β the constant drainage rate. In the case of distributed snow the melt-pond area fraction A_m is given by

$$A_m = \min(1 - A_s, 0.3). \tag{19}$$

Note that for the special case $A_m \to 0$ the formulated growth of melt-pond depth is not representative since $dh_m/dt \to \infty$. However, the effect on the energy budget is negligible (as the contribution to the albedo is proportional to A_m) and the melt-pond depth adjusts rapidly to reasonable values as seen in section 4. For distributed snow, the bare sea ice area fraction is then $A_i = 1 - A_s - A_m$. In the case of uniform-thickness snow, A_m is always 0.3 and A_s or A_i 0.7. In order to avoid unlimited accumulation of meltwater, a maximal melt-pond height of 0.5 m is prescribed following *Taylor and Feltham* [2004]. Excess meltwater simply flows in the underlying ocean.

4. Results

Simulations using the coupled sea-ice-GOTM model were run using observed forcing from 8 May to 3 July 2002 with measured initial conditions for snow and sea ice thickness. Due to the absence of reliable snow precipitation data, a constant snowfall rate of 1.8 mm d^{-1} [*Flato and Brown*, 1996] is prescribed. This rate is the climatological mean snowfall rate at Resolute station. The time period simulated is the same as that considered by *Lavoie et al.* [2005] and *Pogson et al.* [2011].

Four simulations denoted U, UM, R, and RM are discussed here, applying uniform and Rayleigh-distributed snow with and without melt ponds (Table 2). The results are displayed in Figure 4. The relatively coarse spatial (1° × 1°) and temporal resolution (daily-mean) of the CERES cloud data results in overestimates of the model in the incoming solar radiation at the measurement site on some days and underestimates on others (Figure 4a), especially during the solar peak. Forcing the model with the in situ measurements, these biases in under-ice PAR are reduced (not shown). As the intention is to provide large-scale area-averaged light fields for an incorporation in large-scale models, we chose to evaluate the model forced by CERES data. Since we have available observations for only one experiment site to compare with model output which represents areal averages, the comparison is not completely consistent. This is a common problem for model evaluations. Nonetheless, a primary goal of the parameterization is to improve the representation of conditions at the base of the ice during the freeze-melt transition and hence improve the correct timing and size of the ice algal bloom. The comparison suggests an improvement with the use of a snow distribution function versus a uniform snow parameterization.

Results in Figures 4b and 4c show the amount of PAR that reaches the skeletal sea ice layer (the lowest sea-ice model layer). Before 1 June, the mean under-ice PAR in R and RM is about 0.09 W m^{-2} (0.42 μmol photons m^{-2} s^{-1}) and about 0.04 W m^{-2} (0.19 μmol photons m^{-2} s^{-1}) in U and UM (1 W m^{-2} = 4.56 μmol photons m^{-2} s^{-1}, obtained by dividing the average ratio of total quanta to total energy) [*Lavoie et al.*, 2005]. Observations for the same time period show values of about 0.1–0.12 W m^{-2} (0.46–0.55 μmol photons m^{-2} s^{-1}) indicating that R and RM simulations have a much smaller bias than the U and UM simulations. Furthermore, the

Table 2. Simulation Names and the Parameterization Characteristics

Simulation ID	Snow	Melt Ponds
U	Uniform thickness	No
UM	Uniform thickness	Yes
R	Rayleigh distributed	No
RM	Rayleigh distributed	Yes

difference of 0.05 W m^{-2} between uniform-thickness and Rayleigh-distributed snow is significant for ice algal production. Given that the threshold of photosynthetic activity of ice algae in the Arctic is suggested to be about 0.3–1 μmol photons m^{-2} s^{-1} [*Kirst and Wiencke*, 1995], only R and RM simulations allow for a sufficient amount of light for ice algae production before 1 June.

Once melting conditions begin and the snow cover starts to vanish (8 June), large differences between R and U simulated PAR start to emerge. Applying uniform-thickness snow (blue lines), under-ice PAR increases very slowly as the snow thickness decreases. As soon as all the snow is melted (18 June) under-ice PAR jumps from well below 0.5 W m^{-2} to about 10 W m^{-2} for U (blue dotted line) and to about 25 W m^{-2} for UM (blue solid line). Subsequently, the value increases slowly to about 18 and 40 W m^{-2}, respectively, as the sea ice thins. Despite different albedos and the fact that melt ponds are present while snow still remains in UM, differences between U and UM are initially very small. This is because melt ponds form on top of the snow layer, reaching instantly the maximal melt-pond area fraction. This causes melt ponds to be very

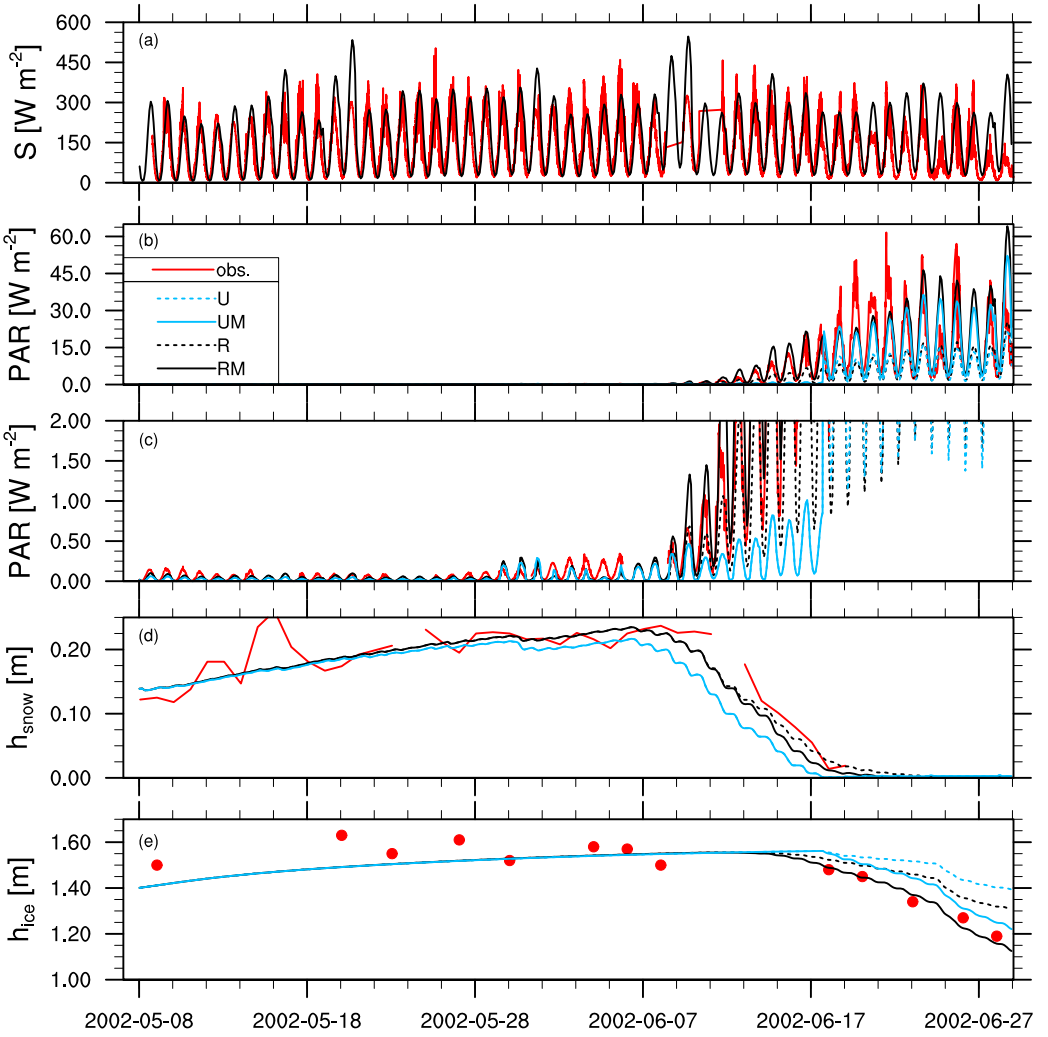

Figure 4. Time series of observations at Resolute, Nunavut, Canada (red) compared to simulations with a Rayleigh-distributed snow cover and melt ponds (black solid), with a uniform-thickness snow layer and melt ponds (blue solid), with a Rayleigh-distributed snow cover and without melt ponds (black dotted), and with a uniform-thickness snow layer and without melt ponds (blue dotted) for (a) incoming shortwave radiation, (b) under-ice PAR, (d) snow thickness, and (e) sea ice thickness. (c) An enlargement of Figure 4b.

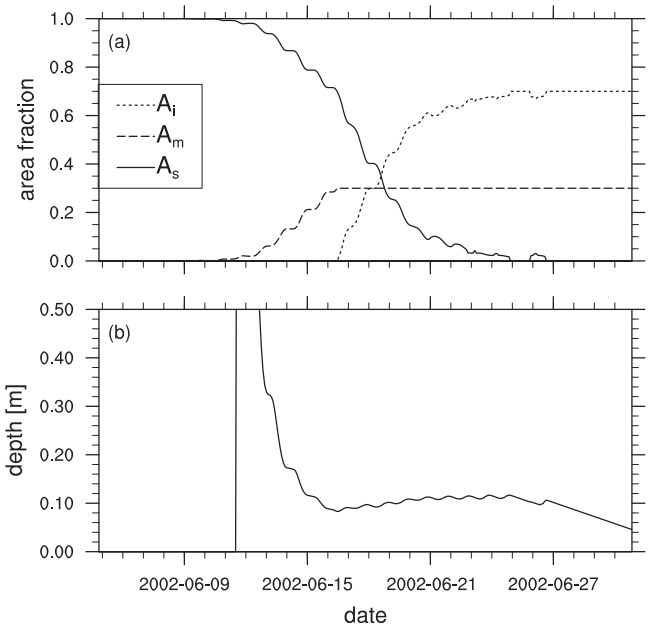

Figure 5. Simulated time series during the melting season of (a) snow area fraction A_s (solid), melt-pond area fraction A_m (dashed), bare sea ice area fraction A_i (dotted), and (b) melt-pond depth for the run with Rayleigh-distributed snow and melt ponds (RM).

shallow at the beginning of the melting season while a fairly thick snow layer still attenuates light effectively. Under Rayleigh-distributed snow, melt pond and bare sea ice areas appear as soon as the snow starts to melt, allowing light to penetrate into the sea ice slab earlier and in larger quantities. While under-ice PAR for R and RM is very similar to that of U and UM runs at the beginning of the snowmelt (8–10 June), only 2 days later substantially larger PAR values (by a factor of three) are reached with a distributed snow thickness, and the difference between U and R (UM and RM, respectively) increases continuously as long as snow is present. For R and RM runs, under-ice PAR reaches values of 10 and 20 W m^{-2}, respectively, 4 days earlier than the values PAR reaches when conditions change from snow covered to snow free in U and UM. For R and RM, this occurs 10 days before the snow has vanished completely (24 June). After all snow has melted, under-ice PAR values for R and RM exceed U and UM by about 2 and 5 W m^{-2}, respectively. These differences occur because the sea ice thickness in the case of distributed snow begins decreasing earlier than under a uniform thickness. A slight overestimation of under-ice PAR in RM compared to observations, in particular during the transition from snow-covered to snow-free conditions (10–18 June), results from an underestimation of the snow thickness caused by an earlier snowmelt onset of about 2 days.

At high light intensities, *Kirst and Wiencke* [1995] suggest values greater than 9 W m^{-2} (about 40 μmol photons m^{-2} s^{-1}) can cause photoinhibition (light-induced reduction in the photosynthetic capacity) in ice algae. Relative to U and UM, this value is exceeded about 4 and 7 days earlier in R (14 June) and RM (11 June), respectively. The potential ice algal production time increases in R and RM due to earlier onsets even though the production time is reduced by about a week within the melting season.

The evolution of the different surface conditions as well as the melt-pond depth of RM is depicted in Figure 5. Areas which are initially snow free are immediately filled with meltwater causing the melt ponds to reach their maximal depth within a day (Figure 5b), which is an artifact of the melt-pond depth parameterization as described in section 3. The melt ponds reach their maximum extent within 6 days (by 16 June). During this time the melt-pond depth decreases continuously to a depth of about 0.1 m by 16 June as the meltwater spreads over a larger area. Once the melt-pond area maximum is reached, bare-ice areas open quickly, accompanied by a slight increase in melt-pond depth to its maximum of 0.12 m at 25 June, the day the snowpack has vanished. Subsequently, melt-pond depth decreases continuously due to the meltwater drainage into the ocean and the assumption that melt ponds form exclusively from snowmelt. Figure 5 shows that the drain rate of melt ponds is so slow that melt ponds remain at the end of the simulation period. The evolution of the three surface types demonstrates the importance of accounting for subgrid-scale snow thickness variability. Even though snow-covered areas persist after 18 June in RM for 6 more days, the under-ice PAR is higher than in UM (Figure 4b) which is snow free by then. This is due to the fact that the increased transmitted radiation in RM allowed for an earlier reduction in sea ice thickness. Figures 4d and 5a indicate that the constant background snowfall has a slight influence on the snowpack evolution, resulting in a slight increase of snow mass and area during nights. This effect has negligible consequences for the under-ice PAR fields because the climatological mean snowfall rate is small compared to the melt rate.

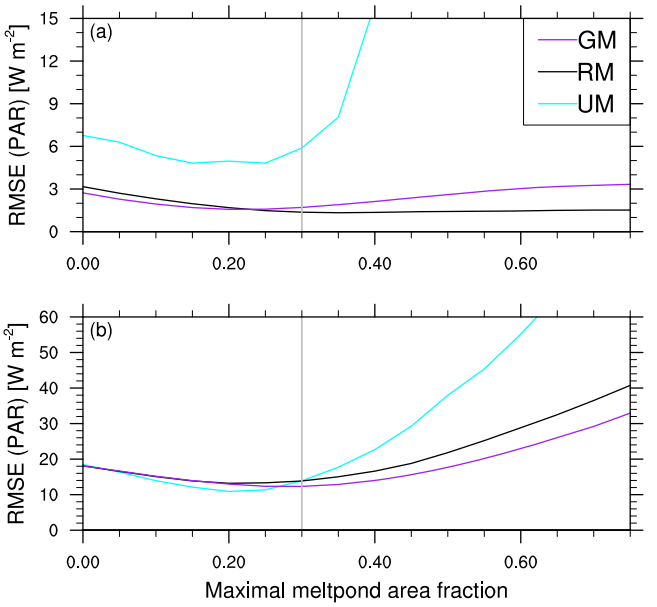

Figure 6. Root-mean-square error of PAR at the ice base dependent on the maximal melt-pond area fraction for simulations with uniform-thickness (UM), Rayleigh-distributed (RM), and gamma-distributed snow (GM) during melting periods (5–21 June) while (a) snow is present and (b) after it has melted. The gray reference line indicates the default value used for the model.

Figure 4 also indicates that the evolution of the mean snow thickness and sea ice slab are better represented under Rayleigh-distributed snow. The gridbox-mean snow thickness decreases more slowly under Rayleigh-distributed snow because the incoming shortwave radiation melts both snow and sea ice, depending on areas of the two surface types. The gridbox-mean snow thickness of uniform-thickness snow is about 3–4 cm thinner than under Rayleigh-distributed snow under melting conditions and disappears earlier (Figure 4d). Effects of the Rayleigh-distributed snow cover on radiative fluxes through sea ice are noticeable for 3 more days in R and 6 more days in RM (21–24 June, respectively). Before melt begins the sea ice thickness evolution is the same in all cases since an effective thermal conductivity for snow under uniform-thickness snow is applied as discussed in section 2. In RM the sea ice thickness begins to decrease about a week before UM (Figure 4e). Therefore, the sea ice thickness during melting for RM is about 10 cm lower. The melt ponds ensure that enough radiation penetrates into the sea ice slab in order to melt the ice at the correct rate (contrast the solid and dashed black lines in Figure 4e).

Results for gamma-distributed snow show very similar behavior to the Rayleigh-distributed snow. Under-ice PAR is slightly higher during the transition time since the snow area decreases slightly faster than under Rayleigh-distributed snow (section 2). Differences between simulations using the two different snow thickness distributions are much smaller than between simulations using distributed and uniform-thickness snow.

4.1. Sensitivity Analyses

The dominant contributions to PAR at the sea ice base during the melting season are from the bare-ice and melt-pond areas. A benefit of the distributed snow thickness parameterization is the explicit prediction of the snow-free area fraction. The maximal melt-pond fraction remains a free parameter which was set to 0.3 in simulations described above. As melt ponds can build up only in snow-free areas the root-mean-square error (RMSE) between observed and simulated ice base PAR during times of melting snow (5–21 June) is weakly sensitive to the maximal melt-pond area fraction (Figure 6a). In contrast, the simulation with uniform-thickness snow is highly dependent on the chosen melt-pond area. Melt-pond areas above 0.35 allow much more light to penetrate into the sea ice slab than observed. After all the snow has melted (Figure 6b), differences between the simulations with different maximal melt-pond area fractions are small. For high maximal melt-pond area fractions UM deviates from other simulations as a result of earlier sea ice loss due to more shortwave energy having reached the ice.

The amount of PAR reaching the sea ice base in the period of interest is sensitive to the total wintertime accumulation for low average snowfall rates. The snowfall rate can vary quite significantly from year to year. At Resolute snowfall rates between 0.7 and 3.5 mm d^{-1} have been observed [*Flato and Brown*, 1996]. While snow remains, changing the snowfall rate over the observed range does not substantially affect the results (Figure 7a), particularly, for snowfall rates higher than the climatological mean of 1.8 mm d^{-1} [*Flato and Brown*, 1996]. The RMSE of light fluxes at the sea ice base for distributed snow is about 2 W m^{-2} smaller than for a uniform-thickness snow. After snowmelt, the RMSE remains weakly dependent on snowfall rates of about 0.8 mm d^{-1} and above. Interannually varying snowfall rates, however, considerably affect the sea ice growth in winter, e.g.,

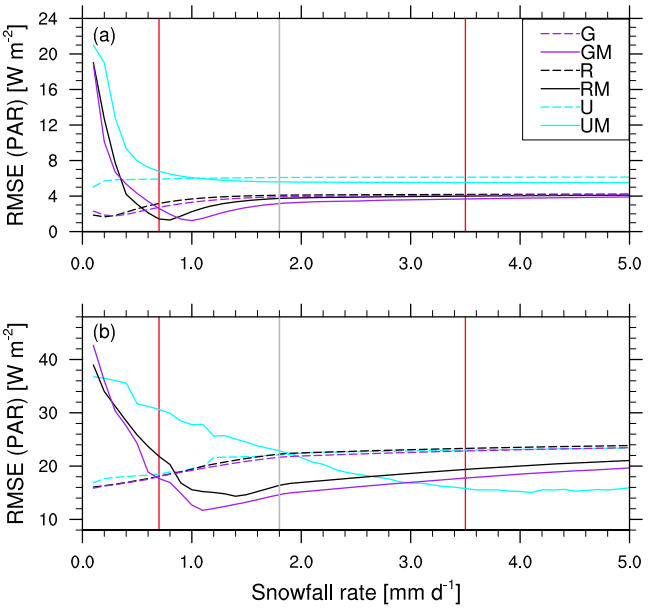

Figure 7. Root-mean-square error of PAR at the ice base dependent on the constant snowfall rate for simulations with uniform-thickness (U), Rayleigh-distributed (R), and gamma-distributed snow (G) with and without melt ponds (M) while (a) snow is present in the melting period and (b) after all the snow has melted. The gray reference line indicates the default value used for the model and red lines indicate the observed range of snowfall rates at Resolute [*Flato and Brown*, 1996].

low snow accumulation reduces the insulation from the cold atmosphere in winter and leads to higher ice growth and delayed ice melt in spring. Hence, an interannually varying snowfall rate is an important factor in representing the observed interannual variability in accumulated sea ice thickness, snow thickness, and summer open water period [*Flato and Brown*, 1996] but does not affect the applicability of the introduced parameterization in the spring-summer transition. The minimum RMSEs are obtained for snowfall rates representative of the particular year under consideration (Figure 7b).

The PAR at sea ice base is also affected by the values used for snow and ice albedo (supporting information), although the sensitivity is weak within realistic ranges of values for these quantities.

5. Discussion

We have demonstrated that the representation of the light field at the sea ice base is more realistic due to the introduction of a snow thickness distribution and resulting surface fractions with different properties during melting. These results suggest several general areas for further investigation.

Generally, all physical processes depending on the thermal field or the gradient of the thermal field are affected by the new parameterization since the thermal field of the sea ice slab is very responsive to the insulating snow cover. For instance, the intensity and depth of brine convection and gravity drainage can be increased [*Notz and Worster*, 2008] which would influence the salinity within sea ice as well as in the ocean surface layer. Changes in salt fluxes due to the higher melting rates, higher internal energy and the increased flushing tend not only to produce thinner ice but also to increase the freshwater supply to the ocean. These processes in turn can affect vertical mixing of the upper ocean. While salt release enhances vertical mixing, under-ice meltwater lenses will strengthen stratification in a similar manner as warming of the upper ocean due to enhanced radiation. So far sea ice salt fluxes have not been coupled to the subgrid-scale snow thickness parameterization, but it would be worth examining the effect of such coupling on these counteracting mixing processes.

This study accounts for melt ponds only as a contribution to the surface energy budget and ignores more detailed melt-pond thermodynamics since this study is focused on the effects of subgrid-distributed snow thickness. *Taylor and Feltham* [2004] demonstrated the importance of the presence of melt ponds on the heat and mass balance of sea ice and the sensitivity of melt-pond depth to drainage rates. The introduced subgrid-scale snow parameterization can be easily combined with more sophisticated melt-pond models [e.g., *Lecomte et al.*, 2011; *Flocco et al.*, 2012; *Hunke et al.*, 2013; Lecomte et al., submitted manuscript, 2014].

The current model does not account for subgrid-scale variations in sea ice thickness. Compared to subgrid-scale snow variations, sea ice thickness distributions have received considerable attention in the modeling community and a detailed discussion of these studies is beyond the scope of this paper [e.g., *Hibler*, 1980; *Bitz et al.*, 2001; *Thorndike et al.*, 2012]. A generalization of the parameterization discussed in this study would correlate snow thickness variations with sea ice thickness variations, as thicker snow is observed to be associated with thicker sea ice. Furthermore, a homogenous snowmelting was assumed which does not reflect natural conditions. *Clark et al.* [2011] demonstrated that accounting for inhomogeneous melting in

subgrid-scale snow thickness distributions changes the rate of snow loss during the melting season, as thicker snowmelts more slowly than thinner snow. This would result in larger snow-free areas building up more quickly at the beginning of the melt season while snow-covered areas would remain longer. Consideration of a more realistic (and observationally constrained) model of the evolution of the snow thickness distribution and a detailed accounting of the physical state of the snow (density, liquid water content, metamorphism, etc.) and its effect on light transmission are interesting directions of future research.

Finally, we would like to point out the need to investigate biological responses to the parameterization introduced here. *Lavoie et al*. [2005] and *Pogson et al*. [2011] found that the timing of ice algal bloom onset and production is highly restricted by the availability of light whereas at the end of the bloom productivity is limited by nutrients. Possible physical process changes as mentioned above will likely affect the nutrient availability within the sea ice and ocean surface. For instance, higher brine convection rates could cause higher concentrations of nutrients within the sea ice. On the other hand, enhanced flushing and earlier ice loss could shorten the time available for ice algal growth, favoring early release of ice algae into the water column [*Fortier et al*., 2002]. While *Lavoie et al*. [2005] focus on bottom ice communities, the improved light conditions during snowmelt can also affect ice communities within the upper ice matrix or in gap layers [*Arrigo*, 2014]. *Tedesco et al*. [2010] provide a modeling example for ice algal growth within a dynamic biologically active layer, allowing growth further up in the sea ice.

In addition to higher light levels during the snowmelt transitions within the sea ice, higher light levels likely also affect the ocean beneath. Intuitively, this could enhance primary production beneath the sea ice [*Arrigo et al*., 2012] or at least initiate earlier blooms. Chl *a* measurements from ice tethered profilers [*Laney and Sosik*, 2014] show under-ice pelagic growth much earlier than typically assumed (as early as February) and it will be interesting to investigate whether the inclusion of snow distribution functions in regional models will allow for earlier under ice growth. Conversely, increased ice algal biomass would induce shading effects reducing the light reaching the sea ice base. This might cause reduced biomass production at the bottom of the ice and within the surface waters, e.g., in the vicinity of the subsurface chlorophyll maximum [*Brown et al*., 2015].

The implementation of the new parameterization into regional sea ice models will also be interesting with respect to impacts on the seasonal sea ice evolution. In addition to possible changes of the vertical structure in the underlying ocean, horizontal effects could be evaluated.

With respect to possible future climate changes and possible shifts in precipitation patterns in the Arctic, we stress the importance in further research on the pdf of snow thickness on sea ice. Available data of spatial snow thickness distributions are scarce and often measured over Arctic multiyear sea ice which has significantly retreated throughout the last decade. More measurements of the actual pdf as well as the spatial decorrelation of snow thicknesses are needed. The spatial decorrelation is important because the gridbox-area average was assumed to be equal to the population mean. If the spatial decorrelation tends to increase in the future or the gridbox sizes decrease dramatically the validity of this approach will weaken.

With respect to large scale and global modeling we recommend replacing the former light penetration equation (equation (3)) by either equation (6) or equation (7) (and the corresponding equations under melting conditions) depending on the preferred distribution. Since most sea ice models already used an effective thermal conductivity for snow, which we have shown results from subgrid-scale snow thickness variations, an introduction of the more accurate conductive heat flux equations (equations (15) or (16)) outside of melting seasons is probably not necessary. This result was shown in section 4 where before the onset of melting the presence of subgrid-scale snow thickness variations had negligible effects on the ice thickness. During melting conditions an accurate partitioning of the surface into areas of snow, sea ice, and melt ponds has a great effect on radiative transfer and energy fluxes (equations (10) or (11) and associated sea ice and melt-pond area fractions). An accurate description of the conductive heat flux through distributed snow thicknesses during melting conditions is not necessary since it is relatively small compared with effects of the albedo change due to melt ponds.

6. Conclusion

This study considers the effect of subgrid-scale snow thickness distributions on light and heat fluxes through sea ice in the context of an idealized formulation intended for use in regional or global models. Simulations

were performed with a coupled one-dimensional sea-ice-ocean model (GOTM with sea ice) and compared to spring observations taken near Resolute (Canadian high Arctic). The principal factor in controlling the amount of light penetrating into the sea ice slab is the snow cover since the extinction and absorption in snow is about an order of magnitude higher than for bare sea ice. Results show the importance of subgrid-scale snow variability to accurately represent the irradiance level at the ice base, as well as the ice and snow thicknesses during the snowmelt transition. The earlier development of snow-free areas as a consequence of snow thickness distributions ensures that the amount of light continuously increases while the snow cover melts. To assess sensitivity of the fluxes to the assumed snow thickness distribution, Rayleigh and gamma distributions were used to describe the snow variability on the subgrid scale. These one-parameter distributions are completely defined by the gridbox-mean snow thickness and yield analytical expressions for the fluxes of light and heat (exact for the former and approximate for the latter). In our parameterization, spatially homogenous melting was assumed across the snow thickness distribution, allowing for areas with thinner snow cover and bare ice to appear already during the melt process and hence ensuring a smooth increase of the under-ice photosynthetically active radiation (PAR) during melting. Subgrid-scale snow thickness distributions allow, therefore, for a dynamic description of the development of the different surface fractions during melting.

In addition, effects of melt ponds on the surface energy budget in snow-free areas were introduced allowing more light to penetrate into the sea ice slab due to their lower albedo. Allowing for a combination of different surface conditions to evolve, defined by the opening of snow-free areas given by the snow distributions, and smoothly transitioning between each as the snow vanishes eliminates the abrupt snow to ice transition in under-ice PAR seen in previous studies. With the new parameterization about twice as much light reaches the sea ice base during freezing periods than under a uniform-thickness snow, thereby halving the root-mean-square error. The comparison of observations with simulations using four different surface parameterizations reveals that after melt onset only a distributed snow cover parameterization is able to capture the observed under-ice seasonal PAR evolution and therefore substantially improves the simulations, particularly, because results are robust against changes in the free parameters of the parameterization. Melt ponds allow about twice as much light to penetrate into the sea ice than without in all simulations. With respect to ice algal production, the snow distribution parameterization allows for an extended temporal range with light levels exceeding minimum light requirements for growth even though the light levels causing photoinhibition are reached somewhat earlier.

The implementation of subgrid-scale snow variability also affects heat fluxes through snow and sea ice, causing higher melt rates than with a uniform-thickness snow. This result agrees well with observations and points out that the largest contribution to changes in the heat fluxes through the surface are from the different surface conditions. Accounting for subgrid-scale snow thickness distributions explains the discrepancy between observed thermal conductivities of snow and those commonly used in sea ice models.

Acknowledgments

We thank Dirk Notz, Greg Flato, and Diane Lavoie for helpful discussions and comments on previous versions of this paper. The authors acknowledge support from the Natural Sciences and Engineering Research Council of Canada (NSERC) CREATE Project on Interdisciplinary Climate Science. A. Monahan further acknowledges support from the NSERC Discovery Grant program and N. Steiner and C. Michel from Fisheries and Oceans Canada. This publication is a contribution to the SCOR working group on Biogeochemical Exchange Processes at Sea Ice Interfaces (BEPSII). We are grateful to two anonymous reviewers for contributing to significant improvements of the manuscript. The snow thickness data used in this paper were acquired from NASA's Operation IceBridge Project (http://nsidc.org/data/idcsi2). Hourly atmospheric data at Resolute, Nunavut, Canada, were obtained from Environment Canada (http://climate.weather.gc.ca). CERES data were obtained from the Atmospheric Science Data Center at the NASA Langley Research Center (http://ceres-tool.larc.nasa.gov/ord-tool/jsp/SYN1degSelection.jsp). For model output, please contact author C. Abraham (carsten.abraham@mpimet.mpg.de), for observational data of PAR, snow, and sea ice thickness at Resolute, contact author C. Michel (christine.michel@dfo-mpo.gc.ca). The model code is currently being implemented into the current GOTM version (http://www.gotm.net/) and will be made available to the public upon completion. Until then please contact author N. Steiner (Nadja.Steiner@dfo-mpo.gc.ca).

References

Abels, G. (1892), Measurements of the snow density at Ekaterinburg during the winter of 1890–1891, *Acad. Nauk Mem.*, *69*, 1–24.

AMAP (2013), *AMAP Assessment 2013: Arctic Ocean Acidification*, viii + 99 pp., Oslo, Norway.

Anderson, M. R., and S. D. Drobot (2001), Spatial and temporal variability in snowmelt onset over Arctic sea ice, *Ann. Glaciol.*, *33*(1), 74–78, doi:10.3189/172756401781818284.

Ardyna, M., M. Babin, M. Gosselin, E. Devred, L. Rainville, and J.-E. Tremblay (2014), Recent Arctic Ocean sea ice loss triggers novel fall phytoplankton blooms, *Geophys. Res. Lett.*, *41*, 6207–6212, doi:10.1002/2014GL061047.

Arrigo, K. R. (2014), Sea ice ecosystems, *Ann. Rev. Mar. Sci.*, *6*, 439–467, doi:10.1146/annurev-marine-010213-135103.

Arrigo, K. R., and G. van Dijken (2011), Secular trends in Arctic Ocean net primary production, *J. Geophys. Res.*, *116*, C09011, doi:10.1029/2011JC007151.

Arrigo, K. R., G. van Dijken, and S. Pabi (2008), Impact of shrinking Arctic ice cover on marine primary production, *Geophys. Res. Lett.*, *35*, L19603, doi:10.1029/2008GL035028.

Arrigo, K. R., et al. (2012), Massive phytoplankton blooms under Arctic sea ice, *Science*, *336*(6087), 1408, doi:10.1126/science.1215065.

Barry, D., J.-Y. Parlange, G. Sander, and M. Sivaplan (1993), A class of exact solutions for Richards' equation, *J. Hydrol.*, *142*(1–4), 29–46, doi:10.1016/0022-1694(93)90003-R.

Bergeron, M., and J.-E. Tremblay (2014), Shifts in biological productivity inferred from nutrient drawdown in the southern Beaufort Sea (2003–2011) and northern Baffin Bay (1997–2011), Canadian Arctic, *Geophys. Res. Lett.*, *41*, 3979–3987, doi:10.1002/2014GL059649.

Bitz, C. M., M. M. Holland, A. J. Weaver, and M. Eby (2001), Simulating the ice-thickness distribution in a coupled climate model, *J. Geophys. Res.*, *106*(C2), 2441–2463, doi:10.1029/1999JC000113.

Brown, Z. W., K. E. Lowry, M. A. Palmer, G. L. van Dijken, M. M. Mills, R. S. Pickart, and K. R. Arrigo (2015), Characterizing the subsurface chlorophyll a maximum in the Chukchi Sea and Canada Basin, *Deep Sea Res., Part II*, In press, doi:10.1016/j.dsr2.2015.02.010.

Burchard, H., K. Bolding, and K. Villarreal (1999), GOTM—A general ocean turbulence model. Theory, applications and test cases, *Tech. Rep. EUR 18745 EN*, Eur. Comm.

Castro-Morales, K., F. Kauker, M. Losch, S. Hendricks, K. Riemann-Campe, and R. Gerdes (2014), Sensitivity of simulated Arctic sea ice to realistic ice thickness distributions and snow parameterizations, *J. Geophys. Res. Oceans*, *119*, 559–571, doi:10.1002/2013JC009342.

Clark, M. P., J. Hendrikx, A. G. Slater, D. Kavetski, B. Anderson, N. J. Cullen, T. Kerr, E. Ö. Hreinsson, and R. A. Woos (2011), Representing spatial variability of snow water equivalent in hydrologic and land-surface models: A review, *Water Resour. Res.*, *47*, W07539, doi:10.1029/2011WR010745.

Corless, R. M., G. H. Gonnet, D. E. G. Hare, D. J. Jeffrey, and D. E. Knuth (1996), On the Lambert W-function, *Adv. Comput. Math.*, *5*(1), 329–359.

Derksen, C., J. Piwowar, and E. LeDrew (1997), Sea-ice melt-pond fraction as determined from low level aerial photographs, *Arct. Alp. Res.*, *29*(3), 345–351.

Domine, F., J. Bock, S. Morin, and G. Giraud (2011a), Linking the effective thermal conductivity of snow to its shear strength and density, *J. Geophys. Res.*, *116*, F04027, doi:10.1029/2011JF002000.

Domine, F., L. Arnaud, J. Bock, C. Carmagnola, N. Champollion, J. Gallet, B. Lesaffre, S. Morin, and G. Picard (2011b), Vertical profiles of specific surface area, thermal conductivity and density of mid-latitude, Arctic and Antarctic snow: Relationships between snow physics and climate, Abstract C32B-01 presented at 2011 Fall Meeting, AGU, San Francisco, Calif., 5–9 Dec.

Donald, J. R., E. D. Soulis, and N. Kouwen (1995), A land cover-based snow cover representation for distributed hydrologic models, *Water Resour. Res.*, *31*(4), 995–1009, doi:10.1029/94WR02973.

Dupont, F. (2012), Impact of sea-ice biology on overall primary production in a biophysical model of the pan-Arctic Ocean, *J. Geophys. Res.*, *117*, C00D17, doi:10.1029/2011JC006983.

Ebert, E. E., and J. A. Curry (1993), An intermediate one-dimensional thermodynamic sea ice model for investigating ice-atmosphere interactions, *J. Geophys. Res.*, *98*(C6), 10,085–10,109, doi:10.1029/93JC00656.

Essery, R. L. H., and J. W. Pomeroy (2004), Implications of spatial distributions of snow mass and melt rate for snow-cover depletion: Theoretical considerations, *Ann. Glaciol.*, *38*(1), 261–265, doi:10.3189/172756404781815275.

Essery, R. L. H., L. Li, and J. Pomeroy (1999), A distributed model of blowing snow over complex terrain, *Hydrol. Processes*, *13*(14–15), 2423–2438, doi:10.1002/(SICI)1099-1085(199910)13:14/15<2423::AID-HYP853>3.0.CO;2-U.

Faria, D. A., J. W. Pomeroy, and R. L. H. Essery (2000), Effect of covariance between ablation and snow water equivalent on depletion of snow-covered area in a forest, *Hydrol. Processes*, *14*(15), 2638–2695, doi:10.1002/1099-1085(20001030)14:15<2683::AID-HYP86>3.0.CO;2-N.

Flato, G. M., and R. D. Brown (1996), Variability and climate sensitivity of landfast Arctic sea ice, *J. Geophys. Res.*, *101*(C11), 25,767–25,777, doi:10.1029/96JC02431.

Flocco, D., D. Schroeder, D. L. Feltham, and E. C. Hunke (2012), Impact of melt ponds on Arctic sea ice simulations from 1990 to 2007, *J. Geophys. Res.*, *117*, C09032, doi:10.1029/2012JC008195.

Fortier, M., L. Fortier, C. Michel, and L. Legendre (2002), Climatic and biological forcing of the vertical flux of biogenic particles under seasonal Arctic sea ice, *Mar. Ecol. Prog. Ser.*, *225*, 1–16, doi:10.3354/meps225001.

Frey, K. E., D. K. Perovich, and B. Light (2011), The spatial distribution of solar radiation under a melting Arctic sea ice cover, *Geophys. Res. Lett.*, *38*, L22501, doi:10.1029/2011GL049421.

Grebmeier, J. M., J. E. Overland, S. E. Moore, E. V. Farley, E. C. Carmack, L. W. Cooper, K. E. Frey, J. H. Helle, F. A. McLaughlin, and S. L. McNutt (2006), A major ecosystem shift in the Northern Bering Sea, *Science*, *311*(5766), 1461–1464, doi:10.1126/science.1121365.

Grenfell, T. C., and G. A. Maykut (1977), The optical properties of ice and snow in the Arctic Basin, *J. Glaciol.*, *18*(80), 445–463.

Hibler, W. D., III (1980), Modeling a variable thickness sea ice cover, *Mon. Weather Rev.*, *108*(12), 1943–1973, doi:10.1175/1520-0493(1980)108<1943:MAVTSI>2.0.CO;2.

Hunke, E. C., D. A. Hebert, and O. Lecomte (2013), Level-ice melt ponds in the Los Alamos sea ice model, CICE, *Ocean Model.*, *71*, 26–42, doi:10.1016/j.ocemod.2012.11.008.

Huwald, H., L.-B. Tremblay, and H. Blatter (2005), A multiyear sigma-coordinate thermodynamic sea ice model: Validation against surface heat budget of the Arctic Ocean (SHEBA)/Sea ice model intercomparison project Part 2 (SIMIP2) data, *J. Geophys. Res.*, *110*, C05010, doi:10.1029/2004JC002328.

Iacozza, J., and D. G. Barber (1999), An examination of the distribution of snow on sea-ice, *Atmos. Ocean*, *37*(1), 21–51, doi:10.1080/07055900.1999.9649620.

Iacozza, J., and D. G. Barber (2009), An examination of the redistribution over smooth land-fast sea ice, *Hydrol. Processes*, *24*(7), 850–865, doi:10.1002/hyp.7526.

Kirst, G. O., and C. Wiencke (1995), Ecophysiology of polar algae, *J. Phycol.*, *31*(2), 181–199, doi:10.1111/j.0022–3646.1995.00181.x.

Kovacs, K. M., C. Michel, B. Bluhm, T. Gaston, R. Gradinger, G. Hunt, S. E. Moore, P. Renaud, and S. Rysgaard (2011), Biological impacts of changes in sea ice in the Arctic, in *Snow, Water, Ice and Permafrost in the Arctic (SWIPA): Climate Change and the Cryosphere*, Arct. Monit. and Assess. Program., Oslo, Norway.

Kurtz, N., M. S. Studinger, J. Harbeck, V. Onana, and S. Farrell (2012), IceBridge sea ice freeboard, snow depth, and thickness, NASA DAAC at the Natl. Snow and Ice Data Cent., Boulder, Colo. [Available at http://nsidc.org/data/idcsi2.html.]

Kurtz, N. T., and S. L. Farrell (2011), Large-scale surveys of snow depth on Arctic sea ice from operation IceBridge, *Geophys. Res. Lett.*, *38*, L20505, doi:10.1029/2011GL049216.

Kwok, R., B. Panzer, C. Leuschen, S. Pang, T. Markus, B. Holt, and S. Gogineni (2011), Airborne surveys of snow depth over Arctic sea ice, *J. Geophys. Res.*, *116*, C11018, doi:10.1029/2011JC007371.

Laney, S. R., and H. M. Sosik (2014), Phytoplankton assemblage structure in and around a massive under-ice bloom in the Chukchi Sea, *Deep Sea Res., Part II*, *105*, 30–41, doi:10.1016/j.dsr2.2014.03.012.

Lavoie, D., K. Denman, and C. Michel (2005), Modeling ice algal growth and decline in a seasonally ice-covered region of the Arctic (Resolute Passage, Canadian Archipelago), *J. Geophys. Res.*, *110*, C04010, doi:10.1029/2005JC002922.

Lecomte, O., T. Fichefet, M. Vancoppenolle, and M. Nicolaus (2011), A new snow thermodynamic scheme for large-scale sea-ice models, *Ann. Glaciol.*, *52*(57), 337–346, doi:10.3189/172756411795931453.

Lecomte, O., T. Fichefet, M. Vancoppenolle, F. Domine, F. Massonet, P. Mathiot, S. Morin, and P. Y. Barriat (2013), On the formulation of snow thermal conductivity in large-scale sea ice models, *J. Adv. Model. Earth Syst.*, *5*, 542–557, doi:10.1002/jame.20039.

Leu, E., J. Wiktor, J. E. Søreide, J. Berge, and S. Falk-Petersen (2010), Increased irradiance reduces food quality of sea ice algae, *Mar. Ecol. Prog. Ser.*, *411*, 49–60, doi:10.3354/meps08647.

Leu, E., J. Søreide, D. Hessen, S. Falk-Petersen, and J. Berge (2011), Consequences of changing sea-ice cover for primary and secondary producers in the European Arctic shelf seas: Timing, quantity, and quality, *Prog. Oceanogr.*, *90*(1–4), 18–32, doi:10.1016/j.pocean.2011.02.004.

Light, B., T. C. Grenfell, and D. K. Perovich (2008), Transmission and absorption of solar radiation by Arctic sea ice during the melt season, *J. Geophys. Res.*, *113*, C03023, doi:10.1029/2006JC003977.

Liston, G. E. (2004), Representing subgrid snow cover heterogeneities in regional and global models, *J. Clim.*, *17*(6), 1381–1397, doi:10.1175/1520-0442(2004)017<1381:RSSCHI>2.0.CO;2.
Liston, G. E., and K. Elder (2006), A distributed snow-evolution modeling system (SnowModel), *J. Hydrometeorol.*, *7*(6), 1259–1276, doi:10.1175/JHM548.1.
Massom, R. A., V. I. Lytle, A. P. Worby, and I. Allison (1998), Winter snow cover variability on East Antarctica sea ice, *J. Geophys. Res.*, *103*(C11), 24,837–24,855, doi:10.1029/98JC01617.
Massom, R. A., et al. (2001), Snow on Antarctic sea ice, *Rev. Geophys.*, *39*(3), 413–445, doi:10.1029/2000RG000085.
Meier, W. N., et al. (2014), Arctic sea ice in transformation: A review of recent observed changes and impacts on biology and human activity, *Rev. Geophys.*, *52*, 185–217, doi:10.1002/2013RG000431.
Mernild, S. H., G. E. Liston, and B. Hasholt (2007), Snow-distribution and melt modeling for glaciers in Zachenberg river drainage basin, north-eastern Greenland, *Hydrol. Processes*, *21*, 3249–3263.
Mernild, S. H., G. E. Liston, D. L. Kane, N. T. Knudsen, and B. Hasholt (2008), Snow, runoff and mass balance modeling for the entire Mittivakkat Glacier (1998–2006), Ammssalik Island, SE Greenland, *Geogr. Tidsskr. Dan. J. Geogr.*, *108*(1), 121–136, doi:10.1080/00167223.2008.10649578.
Michel, C. (2013), Marine ecosystems, conservation of Arctic flora and fauna (CAFF), in *Arctic Biodiversity Assessment: Status and Trends in Arctic Biodiversity*, chap. 14, pp. 486–527, Arct. Counc., Akureyri, Iceland.
Notz, D., and M. G. Worster (2008), In situ measurements of the evolution of young sea ice, *J. Geophys. Res.*, *113*, C03001, doi:10.1029/2007JC004333.
Perovich, D. K., T. C. Grenfell, B. Light, J. A. Richter-Menge, M. Sturm, W. B. Tucker III, H. Eicken, G. A. Maykut, and B. Elder (1999), *SHEBA: Snow and Ice Studies*, version 1.0 [CD-ROM], Cold Reg. Res. Eng. Lab., Hanover, N. H.
Perovich, D. K., W. B. Tucker III, and K. A. Ligett (2002a), Aerial observations of the evolution of ice surface conditions during summer, *J. Geophys. Res.*, *107*(C10), 8048, doi:10.1029/2000JC000449.
Perovich, D. K., T. C. Grenfell, B. Light, and V. Hobbs (2002b), Seasonal evolution of the albedo of multiyear Arctic sea ice, *J. Geophys. Res.*, *107*(C10), 8044, doi:10.1029/2000JC000438.
Perovich, D. K., T. C. Grenfell, J. A. Richter-Menge, B. Light, W. B. Tucker III, and H. Eicken (2003), Thin and thinner: Sea ice mass balance measurements during SHEBA, *J. Geophys. Res.*, *108*(C3), 8050, doi:10.1029/2001JC001079.
Pogson, L., B. Trembley, D. Lavoie, C. Michel, and M. Vancoppenolle (2011), Development and validation of a one-dimensional snow-ice algae model against observations in Resolute Passage, Canadian Arctic Archipelago, *J. Geophys. Res.*, *116*, C04010, doi:10.1029/2010JC006119.
Poulin, M., G. J. C. Underwood, and C. Michel (2014), Sub-ice colonial *Melosira arctica* in Arctic first-year ice, *Diatom Res.*, *29*(2), 213–221, doi:10.1080/0269249X.2013.877085.
Rösel, A., and L. Kaleschke (2012), Exceptional melt pond occurrence in the years 2007 and 2011 on the Arctic sea ice revealed from MODIS satellite data, *J. Geophys. Res.*, *117*, C05018, doi:10.1029/2011JC007869.
Shook, K. (1995), Simulation of the ablation of prairie snowcovers, PhD thesis, Univ. of Saskatchewan, Saskatoon, Canada.
Smith, R. E. H., J. Anning, P. Clement, and G. Cota (1988), Abundance and production of ice algae in Resolute Passage, Canadian Arctic, *Mar. Ecol. Prog. Ser.*, *48*, 251–263.
Søreide, J. E., E. Leu, J. Berge, M. Graeve, and S. Falk-Petersen (2010), Timing of blooms, algal food quality and *Calanus glacialis* reproduction and growth in a changing Arctic, *Global Change Biol.*, *16*(11), 3154–3163, doi:10.1111/j.1365-2486.2010.02175.x.
Steiner, N., K. Denman, N. McFarlane, and L. Solheim (2006), Simulating the coupling between atmosphere–ocean processes and the planktonic ecosystem during SERIES, *Deep Sea Res., Part II*, *53*(20–22), 2434–2454, doi:10.1016/j.dsr2.2006.05.030.
Steiner, N., S. Vagle, K. Denman, and C. McNeil (2007), Oxygen and nitrogen cycling in the northeast Pacific simulations and observations at Station Papa in 2003/2004, *J. Mar. Res.*, *65*(3), 441–469.
Steiner, N. S., et al. (2015), Observed trends and climate projections affecting marine ecosystems in the Canadian Arctic, *Environ. Rev.*, *23*(2), 191–239, doi:10.1139/er-2014-0066.
Sturm, M., J. Halmgren, M. König, and K. Morris (1997), The thermal conductivity of seasonal snow, *J. Glaciol.*, *43*(143), 26–41.
Sturm, M., J. Holgren, and D. K. Perovich (2002), Winter snow cover on the sea ice of the Arctic Ocean at the surface heat budget of the Arctic Ocean (SHEBA): Temporal evolution and spatial variability, *J. Geophys. Res.*, *107*(C10), 8047, doi:10.1029/2000JC000400.
Taylor, P. D., and D. L. Feltham (2004), A model of melt pond evolution on sea ice, *J. Geophys. Res.*, *109*, C12007, doi:10.1029/2004JC002361.
Tedesco, L., M. Vichi, J. Haapala, and T. Stipa (2010), A dynamic biologically active layer for numerical studies of the sea ice ecosystem, *Ocean Model.*, *35*(1–2), 89–104, doi:10.1016/j.ocemod.2010.06.008.
Thorndike, A. S., D. A. Rothrock, G. A. Maykut, and R. Colony (2012), The thickness distribution of sea ice, *J. Geophys. Res.*, *80*, 4501–4513, doi:10.1029/JC080i033p04501.
Vancoppenolle, M., L. Bopp, G. Madec, J. Dunne, T. Ilyina, P. Halloran, and N. Steiner (2013a), Future Arctic Ocean primary productivity from CMIP5 simulations: Uncertain outcome, but consistent mechanisms, *Global Biogeochem. Cycle*, *27*(3), 605–619, doi:10.1002/gbc.20055.
Vancoppenolle, M., et al. (2013b), Role of sea ice in global biogeochemical cycles: Emerging views and challenges, *Quat. Sci. Rev.*, *79*(1), 207–230, doi:10.1016/j.quascirev.2013.04.011.
Vaughan, D., et al. (2013), Observations: Cryosphere, in *Climate Change 2013: The Physical Science Basis. Contribution of Working Group I to the Fifth Assessment Report of the Intergovernmental Panel on Climate Change*, edited by T. F. Stocker et al., pp. 317–382, Cambridge Univ. Press, Cambridge, U. K.
Warren, S. G., I. G. Rigor, N. Untersteiner, V. F. Radionov, N. N. Bryazgin, Y. I. Aleksandrov, and R. Colony (1999), Snow depth on arctic sea ice, *J. Clim.*, *12*(6), 1814–1829, doi:10.1175/1520-0442(1999)012<1814:SDOASI>2.0.CO;2.
Wassmann, P., C. M. Duarte, S. Agustì, and M. K. Sejr (2011), Footprints of climate change in the Arctic marine ecosystem, *Global Change Biol.*, *17*(2), 1235–1249, doi:10.1111/j.1365-2486.2010.02311.x.
Wielicki, B. A., B. R. Barkstrom, E. F. Harrison, R. B. Lee III, G. Louis Smith, and J. E. Cooper (1996), Clouds and the Earth's radiant energy system (CERES): An earth observing system experiment, *Bull. Am. Meteorol. Soc.*, *77*(5), 853–868, doi:10.1175/1520-0477(1996)077<0853:CATERE>2.0.CO;2.
Worby, A. P., M. O. Jeffries, W. F. Weeks, K. Morris, and R. Jaña (1996), The thickness distribution of sea ice and snow over during late winter in the Bellinghusen and Amundsen Seas, Antarctica, *J. Geophys. Res.*, *101*(C12), 28,441–28,455, doi:10.1029/96JC02737.
Zeebe, R. E., H. Eicken, D. H. Robinson, D. Wolf-Gladrow, and G. S. Dieckmann (1996), Modeling the heating and melting of sea ice through light absorption by microalgae, *J. Geophys. Res.*, *101*(C1), 1163–1181, doi:10.1029/95JC02687.